In vitro magnetic hyperthermia using polyphenol-coated Fe_3O_4@γFe_2O_3 nanoparticles from *Cinnamomun verum* and *Vanilla planifolia*: the concert of green synthesis and therapeutic possibilities.

A.L. Ramirez-Nuñez,[a] L.F. Jimenez-Garcia[b], G.F. Goya[c], B. Sanz[d] and J. Santoyo-Salazar [e,*]

[a] Programa de Doctorado en Nanociencias y Nanotecnología, Centro de Investigación y Estudios Avanzados del Instituto Politécnico Nacional, CINVESTAV-IPN, Av. IPN 2508, Zacatenco, 07360, Mexico.

[b] Facultad de Ciencias, Departamento de Biología Celular, Universidad Nacional Autonóma de México, UNAM. Cd. Universitaria, 04510 Mexico.

[c] Instituto de Nanociencia de Aragón and Departamento de Física de la Materia Condensada, Universidad de Zaragoza, 50018 Zaragoza, Spain.

[d] nB nanoSacale Biomagnetics SL, 50012, Zaragoza, Spain.

[e] Departamento de Física, Centro de Investigación y Estudios Avanzados del Instituto Politécnico Nacional, CINVESTAV-IPN, Av. IPN 2508, Zacatenco, 07360, Mexico.

[*]E-mail: jsantoyo@fis.cinvestav.mx

Abstract. We report on a new, environment-friendly synthesis route to produce Fe_3O_4 magnetic nanoparticles (MNPs) from extracts of the plants *Vanilla planifolia* and *Cinnamomun verum.* These aqueous plants extracts have the double function of reducing agents due to their phenolic groups, and also capping materials through the -OH bonding over the MNPs surface. The resulting MNPs have average sizes ≈10-14 nm with a core-shell Fe_3O_4-γFe_2O_3 structure due to surface oxidation driven by the phenolic groups through OH^- covalent bonding. Saturation magnetization values of M_S =70.84 emu/g (*C. verum*) and M_S=59.45 emu/g (*V. planifolia*) are among the largest reported so far from biosynthetic samples. Electron microscopy and infrared spectroscopy data showed a thin organic layer coating the Fe_3O_4@γFe_2O_3 MNPs, composed by the phenolic groups from the starting extracts of both *C. verum* and *V. planifolia.* A proof of concept for these MNPs as heating agents in magnetic hyperthermia experiments (570kHz, 23.9 kA/m) was performed *in-vitro*, showing their efficacy to induce cell death on BV2 microglial cells after 30 min at a target temperature T=46°C.

Key words: green synthesis, iron oxide, magnetic nanoparticles, bioreduction, magnetic hyperthermia.

1. Introduction

Iron oxide magnetic nanoparticles (MNPs) can be obtained by chemical, physical and biological methods (1) improving their properties at low scale. These materials have magnetite core with cubic inverse spinel structure, oxygen forming *fcc* close packing and divalent Fe^{+2} ions occupying tetrahedral sites and trivalent Fe^{+3} ions in octahedral sites (2). Deviations from the ½ Fe^{+2}: Fe^{+3} of the pure magnetite phase by oxidation of Fe^{2+} to Fe^{3+} usually results in γ-Fe_2O_3 (maghemite phase) at the nanoparticle's surface. Maghemite is a cation-deficient spinel represented by the formula $[Fe^{3+}]_A[Fe^{2+}{}_{1-3X}Fe^{3+}{}_{1+2X}\square_X]_BO_4$ where $\square$ represents iron vacancies originated during the synthesis process and/or subsequent oxidation. Typically, surface oxidation of Fe_3O_4 MNPs would result in a Fe_3O_4@γ-Fe_2O_3 core-shell structure. These MNPs have high potential in the biomedical field, mainly for drug delivery (3), magnetic resonance imaging (4) and magnetic hyperthermia (5).

This wide range of applications has motivated the development of quite a large number of synthesis routes including ion-sputtering (6), sol-gel technique (7), mechano-chemical activation (8), co-precipitation (9), laser ablation (10), hydrothermal (11) and ultrasonic (12). To ensure biocompatibility for biomedical applications, these methods require tedious separation procedures to remove hazardous chemicals at their surface from reactants or byproducts of the synthesis route (13) and thus developing a safe, ecofriendly approach has been a challenge of nanotechnology research (14). In recent years eco-friendly synthesis of metallic nanoparticles has been reported (15, 16) based on the use of green materials like biomass, plant extracts or reducing biomolecules, a process known as bio-reduction or biosynthesis (17). A list of the metallic nanoparticles obtained by biosynthesis employing plants biomass or extracts are available in reviews, reported by Amit *et al.* (15), Mohanpuria *et al.* (18), Herlekar *et al.* (19) and Quester *et al*. (20). Regarding the synthesis of MNPs, strategies using living plants (14, 21, 22), dried plant biomass or their extract (14) have been proposed. Compared to biological synthesis (i.e., using fungi, microorganisms, mammalian cells or enzymes) the plants aqueous extracts are advantageous because they do not require elaborate processes for maintaining cell cultures and are easy to scale up (17).

Successful synthesis of iron nanoparticles have been reported using tea leafs (23, 24), alfalfa biomass (25) and sorghum bran extracts (26). Plant extracts provide the reducing agents from a natural source in replacement of the generally more toxic synthetic reactants (15, 27). There are many plant extracts containing biomolecules with alcoholic functional groups that influence the final Fe_3O_4 MNP morphology (20, 28). Active biological phytochemicals components (i.e., polyphenol compounds, tannins, flavonoids, carbohydrates etc.) present in aqueous plant extracts act as reducing and capping agents during MNP growth (18, 22) and, depending on the

concentration of phytochemicals of each plant, can react onto metal ions in shorter times (minutes to hours) compared to similar molecules from microorganisms (14, 29, 30).

Some of the biomolecules present in extracts of *C. camphora* have a protective role and might also influence the final shape of Au and Ag nanoparticles synthesized from their biomass (28). These biomolecules in aqueous medium act as capping agents avoiding the collapse of growing nanostructures, while the polyol and soluble heterocyclic components are mainly responsible for the bio-reduction of metallic ions in solution (28). In general, the resulting organically-coated surfaces with bioactive properties is one of the main advantages of biosynthetic routes for MNPs, making this synthesis strategy useful for biomedical applications (31). Their lower toxicity has been profited to use these MNPs as contrast agents in magnetic resonance imaging (MRI) constituting an improvement over conventional iodine-based contrast agents (31),(32).

Polyphenols have received substantial attention for neuroprotective therapies based on the known anti-oxidative and anti-inflammatory properties of flavonoids and catechins (33-35). On a molecular level, the potential therapeutic effects of these molecules to age-related brain diseases is related to their capacity to deter the functional degeneration of amyloid-β peptides in diseases like Alzheimer, Parkinson´s and amyotrophic lateral sclerosis. There is already reported evidence *in vivo* regarding the protective effects of flavonoids in Parkinson's and Huntington's diseases (33, 35). There is consensus on the fact that these molecules can slow/impede the proliferation of amyloid-β peptides and/or transformation into neurotoxic aggregates. In addition, there are reports on the use of MNPs as carriers of polyphenols *in vitro* that demonstrated antineoplastic efficacy of curcumin conjugates on breast cancer, glioma, and pancreas xenografts models (36). From these considerations, naturally-produced MNPs with polyphenol surface coatings are expected to contribute to new therapeutic strategies (33). Green synthesis of MNPs is an alternative scarcely explored for hyperthermia treatment, mainly due to high-cost production and immunological reactions of MNPs from bacterial origin (19). Plant based synthesis especially those from their extracts offer a promising alternative. Their essential oils contain small hydrophobic terpenoid or phenolic compounds that can easily permeate cell membrane,(37) becoming an alternative accessible and renewable carbon source for the synthesis of metallic nanoparticles. Previous reports have shown some control on the final sizes and morphologies (spherical, platelets, and nanorods) of MNPs by control within the aqueous extracts (pH, temperature, inert atmosphere, etc.) and, for polyphenols, a key control parameter is concentration during processing (14, 17, 30).

Here, we report on the viability of polyphenols and organic acids to obtain MNPs, exemplified in two different systems synthesized by an eco-friendly method in aqueous extracts of: (1) *Cinnamomun verum* and (2) *Vanilla planifolia* (natural and synthetic). We show that this is an easy and environmentally clean synthesis route for MNPs, and we present a complete characterization of their physical properties and provide a proof of concept *in vitro* for their

potential application in magnetic hyperthermia.

2. Materials and methods.

2.1 Materials.

Ferric trichloride hexahydrate ($FeCl_3 \bullet 6H_2O$) (reagent grade, ≥98%) and ferric dichloride tetrahydrate ($FeCl_2 \bullet 4H_2O$) (puriss, p.a., ≥99%) and sodium hydroxide (NaOH) (reagent grade, ≥98%) were purchased from Sigma-Aldrich Reagent Co., all reagents were used directly without further purification. *C. verum* (Sri Lanka) and *V. planifolia* cured pods were obtained from local market in Mexico. Vanilla commercial concentrated extract (SV) was obtained from "La Reyna", Jose Acateno and Papantla Ver. Mexico region. Deionized water (resistivity=18 MΩ.cm) was used in all experiments.

2.2 Cinnamon and vanilla natural extract preparation.

Starting natural materials used were cinnamon bark dried and cured vanilla pods, since previous reports showed that dried leaves enhance the extraction process and produce extracts with better antioxidant properties than non-dried leaves (24, 38). A low cost, ecofriendly route was developed so that extraction solvents were prepared easily in aqueous solution media. Additionally, the resulting solvents exhibited a high capacity to extract polyphenols safely (39). Dried and grinded *C. verum* bark powder (50 g), was mixed with 200 ml of deionized water and treated for 3 h at 80°C by steam distillation. After settling to cold down to room temperature, cinnamon aqueous extract (C) solution was filtered through Nylon 0.22 um filter to remove cellular debris, and stored for a week at 4°C for further use. For vanilla extract (VP) 10 grams of *Vanilla planifolia* cured beans were extracted by the same procedure until the color of aqueous solution changed from watery to yellow. The extract with the volatile oil was filtered and stored as the former.

2.3 Synthesis of Fe_3O_4 MNPs.

Fe_3O_4 MNPs were synthesized by a green co-precipitation method (40) with some modifications. A starting solution of 0.02 M $FeCl_3 \bullet 6H_2O$ and 0.01 M $FeCl_2 \bullet 4H_2O$ were dissolved separately in deionized water for 30 minutes. Subsequently ½ Fe^{+2}: Fe^{+3} solution was mixed and fulfilled to 100 ml with deionized water and controlled heating at 80°C under agitation and atmospheric pressure under N_2 atmosphere. When the temperature was reached, 5 ml of the aqueous extract was added drop wise. The color of the solution changed to reddish-brown. After 30 minutes 1.5 M NaOH was added continuously to allow the uniform precipitation of black MNPs. The mixture was rapidly cooled down with ice, and MNPs were obtained by magnetic decantation. Final MNPs either cinnamon (C-MNPs), vanilla pods (VP-

MNPs) aqueous extracts or commercial/synthetic vanilla (SV-MNPs), were washed tree times with deionized water until pH 7 was reached. The iron contents in all samples were measured through a thiocyanate complexation assay. In order to compare green synthesis performance, a chemical synthesis method was done by using tetraethylammonium hydroxide (A-MNPs).

2.5 Physical characterization

Magnetization hysteresis loops were measured for all samples using a vibrating sample magnetometer (VSM, Lake Shore 7400 Series) at room temperature. The hysteresis loops, M_S (emu/g) *vs* H (Oe) were acquired for applied fields $-12{,}000 \leq H \leq +12{,}000$ Oe. The topography and magnetic domains analysis of nanoparticles surface were done by using scanning probe microscope (SPM) JEOL-JSPM-5200 in AFM-MFM Magnetic Force Microscope (MFM) mode. For each sample, powder was confined in a carbon adhesive tape (41). Magnetic tip NSC14, Co-Cr/15 Micromasch was previously magnetized to record the magnetic domains at 180 KHz with lift height interaction of 0-18.605 nm and output of 0.025 Amp/V. The 2D and 3D images, profiles and domains measurements were processed with WinSPM Process version 2.0 software JEOL Ltd.

X-ray diffraction (XRD) patterns of Fe_3O_4@Fe_2O_3 MNPs powder were obtained in a Rigaku diffractometer (Rigaku-Smart Lab) equipped Cu Kα radiation with wavelength of 1.54 Å operating at 35 kV acceleration voltage and current of 25 mA. The data were collected with Bragg angle 2θ in range 10^o - 80^o at a scanning rate of 0.02 °/s. The diffraction patterns were compared with the Data Base Powder Diffraction File, JCPDS-PDF PDF-19-0629, release 2012, International Center for Diffraction Data ICCD (42). The average crystallite size was estimated using the Debye-Scherrer's formula ($d=0.9\ ^{a}/\ \cos\theta$), were d is the crystal size, λ is the wavelength for CuKα, K the constant shape (0.89) and is the full width at half maximum (FWHM). PowderCell 2.0 software was used to compare the experimental and theoretical data for d value calculation, corresponding to PDF-19-0629; inverse spatial group *Fd3m* (227) inverse spinel FCC structure.

2.6 Determination of iron contents in the magnetic colloids.

The Fe concentration was determined by UV-Vis spectrophotometry through the thiocyanate complexation reaction (43, 44):

$$Fe^{3+}_{(aq)} + 6SCN^-_{(aq)} \longrightarrow \left[Fe(SCN)_6\right]^{3-}_{(aq)}$$

MNPs were dissolved in HCl 6 M-HNO_3 (65%) at 50°C during 2 hours until the complete oxidation of Fe^{2+} ions to Fe^{3+}. Potassium thiocyanate 1.5 M was then added to the Fe^{3+} solution to form the iron-thiocyanate complex, which has a maximum absorbance at 478 nm wavelength.

The iron concentration was determined by comparing the sample absorbance to a calibration iron curve (44).

2.7 Specific power absorption (SPA) measurements.

The SPA of the *as prepared* magnetic colloids was measured by triplicate in a commercial ac applicator (DM1, nB nanoscale Biomagnetics, Spain), with field amplitudes H_0 in the range 3.97 k $Am^{-1} \leq H_0 \leq$ 23.9 k Am^{-1} (1 Oe = 79.5775 Am^{-1}) at fixed frequency f = 570 kHz. *In vitro* experiments were performed in BV-2 cells at fixed frequency f=570 kHz, with an experimental setup designed for constant target temperature T = 46 °C, achieved by a feedback control of the field intensity H_0. The samples were conditioned into a quasi-adiabatic space of small volume (~0.5 ml) forming compact pellets of 2-8×10^6 cells. The power released by the magnetic colloid per unit of mass of iron oxide content is given by the specific power absorption (SPA) expressed in W/g $_{Fe3O4}$. The SPA is the rate of energy converted into heat per unit mass of magnetic material subjected to an alternating magnetic field (45), and can be calculated as:

$$SPA = \frac{\delta_l \, c_l}{\phi} \left(\frac{\Delta T}{\Delta t}\right)_{max} \quad \text{Eq. (4)}$$

where δ_l is the density of the carrier liquid (i.e. water) and c_l its specific heat capacity (c_{water}= 4.18 J/g. K); ϕ is the MNPs mass concentration $\phi = m_{NP}/V_l$ of the colloid containing a mass of nanoparticles m_{NP} (in mg) in a volume V_l (in mL). The SPA per gram of the magnetic colloid, was obtained from the initial slope of T *vs.* time data, after the ΔT increment during the first $\Delta t \approx$ 10-20 seconds were measured (45).

2.8 Cell culture.

Immortalized brain microglia murine cell line BV-2 (ATCC®CRL-2467™) were cultured in Dulbecco´s modified Eagle´s medium supplemented with 10 % fetal bovine serum, 100 IU/ml penicillin, 100 µg/ml streptomycin and 2 mM L-glutamine. Cells were maintained at 37 °C in saturated humidified atmosphere containing 95% air and 5% CO_2.

2.9 Cell viability assays.

For the viability assays, 3 x 10^5 cells in exponential growth phase were seeded into a 6 well plate and incubated for 24 hour as described previously. The experiments were done by triplicate. The culture media was added with increasing MNPs concentrations (25, 50 and 100 µg/ml) and incubated for 24 h. After 48 h cells were harvested and trypan blue staining was performed to estimate live (none-stained) and dead (blue-stained) cells number. In the assay 30

μl of cell samples were diluted into 2% Trypan blue dye (1:1). The viable and non-viable cells were counted in a Neubauer chamber (Blau Brand Germany, 718605). Cell density and viability was calculated according to Calatayud *et al.* 2014 (44). The adhered cells to the culture plate and none-adhered cells were considered in the calculations.

2.10 Quantification of uploaded MNPs by BV-2 cells.

In order to evaluate the MNPs cellular uptake, 3 x 10^5 cells were seeded into 6 well plate by triplicate. After 24 h of incubation the media was replaced and cells were co-incubated with increasing amount of MNPs (0, 25, 50 and 100 μg/ml). At 48 h the cells were harvested and washed with PBS (3 x 2ml), tripsinized, and accounted by trypan blue assay (only adhered cells). Then the pellet was washed with MilliQ water and centrifuged (1200 RPM) to completely remove media. The pellet was digested in HCl 6 M-HNO_3 (65%) solution for thiocyanate assay and the amount of uptaken (incorporated or strongly membrane bound) MNPs by BV-2 cells was quantified by UV-VIS absorption spectroscopy. The doubling time (T_D) of BV2 cells was determined in order to assess the optimal incubation range interval with MNPs (46).

2.11 Alternating Magnetic Field Measurements (AMF).

For hyperthermia *in vitro* experiments BV-2 cells were grown up to confluent state into a 75 cm^2 culture flask. Cells were cultured overnight at 37 °C with 100 μg/ml of MNPs. The next day cells were washed PBS (3 x 2ml), detached, centrifuged and re-suspended in 150 μl of complemented DMEM in a PCR tube. Each sample consisted of >1.8 x10^7 cells. To provide a precise control of the heat delivered during magnetic hyperthermia (MHT) experiments a concentration of 100 μg/ml of MNPs was tested seeding 3x10^6 cells previously. Cell pellets undergone an AMF treatment in a commercial ac applicator (model DM100 by nanoscale Biomagnetics S.L., Spain) working at fixed f= 570 kHz and field amplitude of 300 Gauss (23.9 kA/m) with a constant target-temperature program feedback at 46 °C set-point for 30 minutes. Temperature was maintained through a feedback-based controller field amplitude modulation. The applicator is equipped with an adiabatic space (~ 0.5 ml) for measurements in liquid phase. Temperature was measured using a fiber-optic thermometer and placed in the center of the pellet. After MHT test, cells were sub-cultured for 6 h. Then cell viability was determined by Trypan blue assay. Finally iron concentration was measured through thiocyanate assay by UV-VIS.

2.12 Transmission Electron Microscopy and Dual Beam FIB-SEM.

a) Magnetite samples were diluted in ethanol 70% and sonicated 15 min. Drops of samples were supported in formvar carbon copper grids and were observed by Transmission Electron Microscopy (TEM) JEOL, JEM2010, LaB_6, at 200keV at CINVESTAV-IPN and FEI Tecnai T20, at 200 keV at INA-UNIZAR. The average particle size was determined by measuring the largest dimension in 200 particles. Their distribution was fitted to Gauss function.

b) The cells subjected to MHT experiment were fixed with glutaraldehyde (4%) at 4 °C for 2 h. Then washed once with cacodylate buffer (0.2M, pH=7.2) and resuspended in glutaraldehyde (2%) at 4 °C for 4 h. Then were postfixed 1 h with 2% osmium tetraoxide containing 2.5% potassium cyanoferrate, and gradually dehydrated in acetone (30-100%). Staning was carried out with uranyless in acetone 50% during dehydration and finally embedded in Epoxi resin. Thin sections (70 nm) were placed onto 200 mesh copper grids, and counterstained with lead citrate before examination with a FEI Tecnai T20 Transmission electron microscope at 200 kV.
For dual beam FIB-SEM a drop of the dehydrated samples was placed in a cover slip and sputter coated with gold-platinum. SEM images were recorded at 5 and 30 kV using a FEG column. A combined Ga-based 30kV (0.4 nA) ion beam was used to cross section single cells. EDS-X spectrometry was performed to identify intracellular iron nanoparticles.

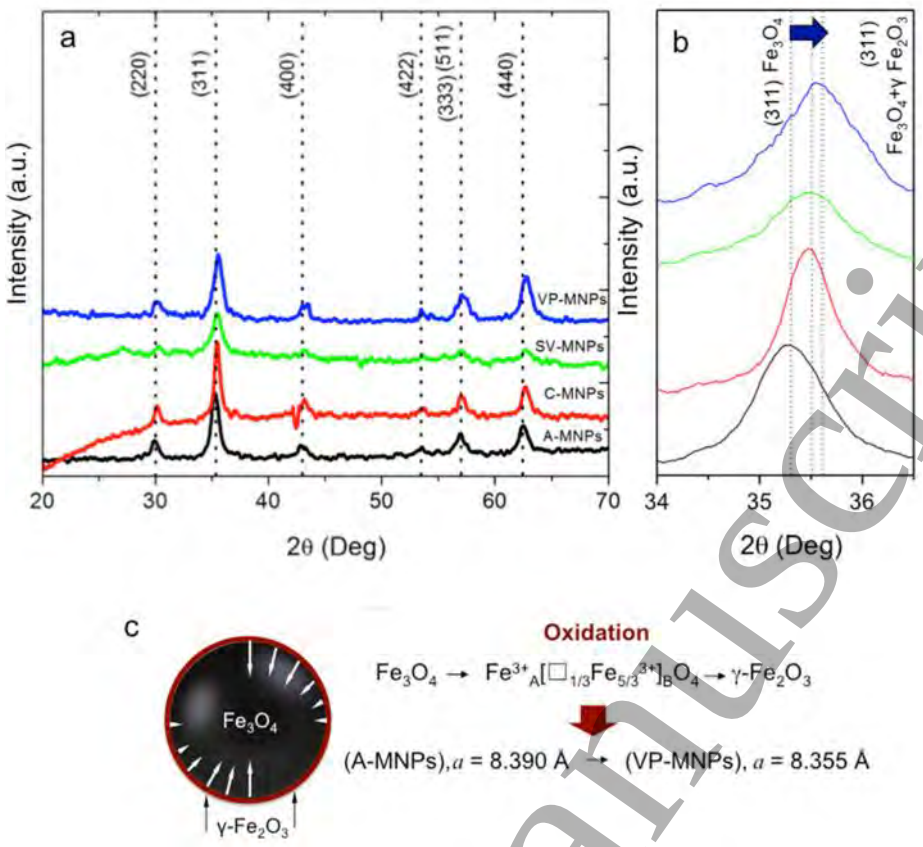

Figure 1. a) XRD patterns of Fe_3O_4@Fe_2O_3 MNPs from aqueous extracts of *C. verum* (C-MNPs); *V. planifolia* vanilla pods (VP-MNPs) and synthetic vanilla (SV-MNPs). b) Amplification of the 2Θ ≈35.5º region showing the shift of the diffracted (220), (311), (400), (422), (511) and (400) crystallographic planes from the expected values for Fe_3O_4 in A-MNPs (not oxidized) to the γ-Fe_2O_3 in phenolic-coated MNPs. c) A schematic representation of the surface oxidation of VP-MNPs.

3. Results

3.1. Physical properties of the MNPs

The XRD analysis of all samples (C-MNPs, VP-MNPs and SV-MNPs) showed the main magnetite peaks (A-MNPs) (2θ positions at 30º (220), 35.19º (311), 43º (400), 53º (422), 57º (333,511) and 62º (440) (Figure 1a). These peaks were found to be slightly displaced (Figure 1b) to maghemite (47) likely originated from surface oxidation during the synthesis (Figure 1c). The main crystalline growth orientation was the (311) diffraction plane. A non-linear slope in the baseline of the patterns was observed, assigned to the non-crystalline contribution from remaining biomolecules in the samples due to covalent bonding between iron ions and polyphenols during reduction, growth and capping of MNPs (Figure 1a). The mean particle sizes $< d >$, estimated from broadening of the main XRD peaks, were $< d > = 14\ nm$ for C-MNPs (*C. verum)* and $< d > = 12\ nm$ for SV-MNPs and VP-MNPs (*V. planifolia* synthetic vanilla and pods extract, respectively).

A specific feature of the present synthesis method is that the phenolic biomolecules of the natural extracts used yield the formation of surface-oxidized magnetite MNPs, i.e., a core-shell Fe_3O_4-γFe_2O_3 configuration. This oxidation is expected from the concentration of phenols in the starting biomass and consistent with the small changes of the (average) unit cell parameters: *a*= 8.355 Å in -*VP-MNPs,* and *a*=8.366 Å in *C-MNPs* (see Table 1). These changes with respect to the parameters of Fe_3O_4 are consistent to the Fe^{2+} vacancies of the γ-Fe_2O_3 structure at the MNPs surface. This oxidation is expected since the extract concentration used during synthesis can oxidize the MNP surface and produce Fe vacancies during processing. A consequence of this oxidized γ-Fe_2O_3 layer at the MNPs surface is a higher stability both in time and against chemical attacks, a clear advantage for potential biomedical applications (48).

Table I. Physical parameters of Fe_3O_4@Fe_2O_3 MNPs

Sample	**Plant extract**	**Base**	**particle size (nm)**		**cell parameter (Å)**		**domain size (nm)**			
			XRD	TEM	XRD	TEM	MFM	H_c (Oe)	M_S (emu/g)	SPA (W/g_{Fe3O4})
A-MNPs	None	$(CH_3CH_2)_4NOH$	13	13.3 ± 1.4	8.390	8.374	4.0	8.66	68.16	195.0 [a]
C-MNPs	Cinnamon (C)	NaOH	14	14.4± 3.5	8.366	8.382	5-6	62.81	70.84	335.69
SV-MNPs	Synthetic vanilla (SV)	NaOH	12	14.0± 3.1	8.365	8.387	2-3	37.54	60.80	78.9
VP-MNPs	Vanilla pods (VP)	NaOH	12	10.2± 2.7	8.355	8.372	3.5	13.71	59.45	234.0

[a] From reference (49)

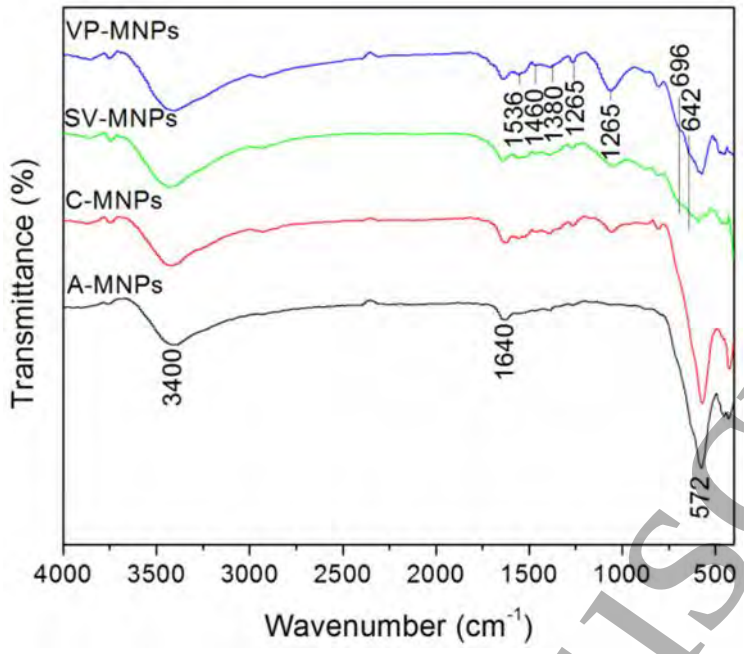

Figure 2. FTIR spectra of MNPs synthesized with C and VP extracts. The bands at 1536 to 1060 cm^{-1} indicate the presence of aromatic compounds on the MNPs surface.

The FT-IR spectra (Figure 2) showed the vibrational stretching mode of Fe-O bond at 572 cm^{-1} characteristic of magnetite (Fe_3O_4), oxide phase formation (50). The broad area band absorption at 3400 cm^{-1} is due to stretching vibrations from O-H bonding. The associated peak at 1536 cm^{-1}, indicates the chemical compound is likely to be a simple hydroxyl compound (phenol). The C-H stretching vibrations (3000 cm^{-1}) overlap the stretching vibration of O-H. The set of lower frequency bands in the range from 1536 to 1060 cm^{-1}, are consistent with unsaturated bonds (C=C) from aromatic compounds, due to phenol groups or quinone. These are involved as electron donors during the bio-reduction process (51). Between this set aldehyde groups (C-H torsion) at 1380 cm^{-1} and carboxylic acids (COO-) at 1460-1265 cm^{-1} signals are located. The band at 1640 cm^{-1} is associated to carbonyl groups from organic base in chemical synthesis (A-MNPs). The surface oxidation of VP-MNPs and SV-MNPs was promoted in SV and VP extracts as observed by band splitting and displacement from 572 cm^{-1} to 642 cm^{-1} in VP-MNPs and 696 cm^{-1} in SV-MNPs. Whereas A-MNPs and C-MNPs remained at 572 cm^{-1} meaning that C natural extract exerted a better protective oxidation effect.

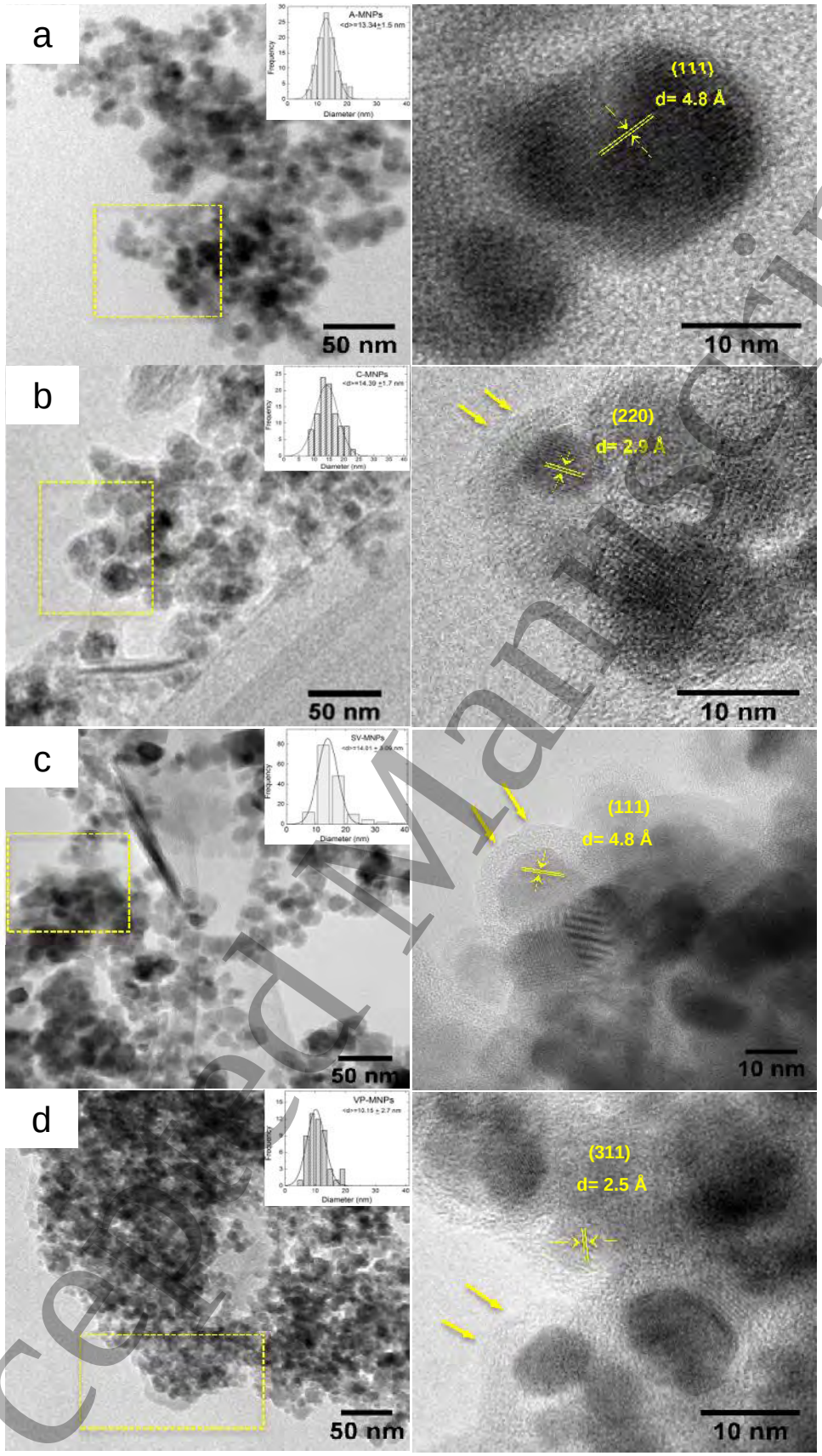

Figure 3. TEM micrographs of MNPs synthetized with (a) tetraethylammonium hydroxide (b) C aqueous extract (c) SV extract and (d) VP aqueous extract. In all synthesis with extracts, particles are surrounded by an external organic coating (arrows, zoom in images), which slightly decreases their agglomeration. Histograms of mean particle size diameter values were fitted with a Gaussian function.

The morphology and size of the $Fe_3O_4@\gamma Fe_2O_3$ MNPs observed in transmission electron microscopy (TEM) images showed a common quasi-spherical (spheres with irregular borders) morphology of all MNPs (Figure 3). For C-MNPs, SV-MNPs and VP-MNPs an amorphous surface layer of t≈5-9 nm thickness (yellow arrows in Figure 3b, c and d) corresponding to polyphenols from the aqueous plant extract, in agreement with the spectral evidence from FT-IR.

The polymer layer around the C-MNPs magnetic cores was thinner (t=3.45 nm) than for VP-MNPs (t=5.98-8.54 nm). The mean particle sizes <d> as calculated from the fit of size histograms were 14.39±1.7 nm in C-MNPs (from cinnamon extract), 14.01±3.0 nm in SV-MNPs (from synthetic vanilla) and 10.15±2.7 nm in VP-MNPs (from vanilla pods extract). All within the particle size range of a chemical synthesis using tetraethylammonium hydroxide (A-MNPs) as a reducing agent (Table 1). The narrower particle size distribution was obtained with vanilla commercial extract, maybe due to a higher concentration of synthetic polyphenols or food additives commonly used in commercial vanilla products (52). This size distribution was similar to common synthetic nanoparticles from chemical synthesis (A-MNPs), where highly purified substances are used. Meanwhile both C and VP aqueous extracts yielded a wider particle size distribution. This effect could be attributed to the complex mixture of biomolecules (polyphenols, reducing sugars, etc.) common in aqueous extracts (15, 24, 26). Those in turn also allowed the formation of several nanoparticles shapes as reported by other biosynthesis methods using different plant aqueous extracts (28, 53). The reducing power of polyphenols mixture in Fe^{+2} iron solution has an effect in the lattice as compared with A-MNPs parameter (d=4.848 Å). Those have interplanar distances of d=4.792 Å in C-MNPs, d=4.848 Å in CV-MNPs and d=4.798 Å in VP-MNPs, all associated with the plane (111). Chemical synthetic polyphenols in commercial extract allowed the formation of crystalline phases closer to magnetite structure; meanwhile aqueous natural extracts oxidize the surface yielding magnetite-maghemite MNPs, due to the additional water molecules from the extract.

The hysteresis loops M_S (emu/g) *vs* H (Oe) at room temperature (Figure 4) of all samples showed a superparamagnetic state of the MNPs, as expected for single-domain configurations of these sizes. A small contribution to the coercive field H_C (see Table 1) can be noticed, and could be originated in larger magnetic anisotropy and/or the contribution of larger particles within the size distribution. The saturation magnetization M_S values from the curves are also displayed in Table 1. The largest value corresponded to C-MNPs sample (*C. verum* extract, M_S= 70.84 emu/g), consistent with the more ordered crystal structure of the magnetic core observed in HRTEM images. In VP-MNPs (vanilla pods), the sample has the smallest average particle size, the saturation value M_S=59.45 emu/g was the lowest and thus this is likely to be related to

surface effects. We note that since the average particle sizes are around 15 nm, it is possible that the different phenolic capping layers on different samples could also have influence on the surface ordering of the γ-Fe_2O_3 magnetic moments.

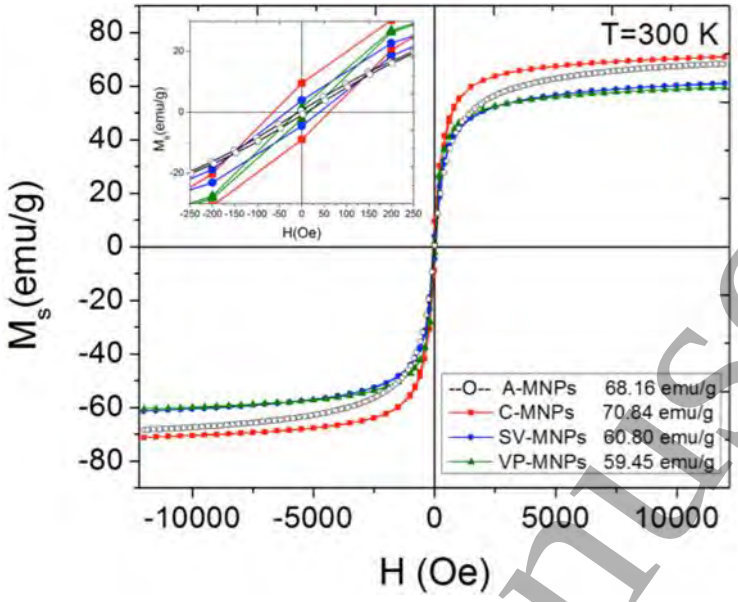

Figure 4. Hysteresis loops Fe_3O_4@γ-Fe_2O_3 MNPs measured at 300 K. Left inset: enlargement of the coercive field for each synthesis.

This influence of the capping materials on the surface spin order has been reported for several MNPs with silica, dextran and starch coatings (31). All in all, the present values of M_S compare well with other reported values from MNPs biosynthesis: M_S=55.4 emu/g using *Mimosa pudica* (54); M_S=22.1 emu/g from *Sargassum muticum* (55); M_S=13.2 emu/g using *Passiflora tripartite var. (56)*; M_S=37.1 emu/g in soya bean sprouts (57); M_S = 68 emu/g from *Aspergillus niger* fungi (58); M_S=15.8 emu/g from Plantain peel extract (59); M_S=13.6 emu/g from *Sysygium cumini* (60) or M_S=48.77 emu/g from marine bacteria *Shewanella sp.* (61). Indeed, to the best of our knowledge, the present C-MNPs obtained by the one–step reaction from *Cinnamon verum* extracts have the highest M_S = 70.84 emu/g reported so far.

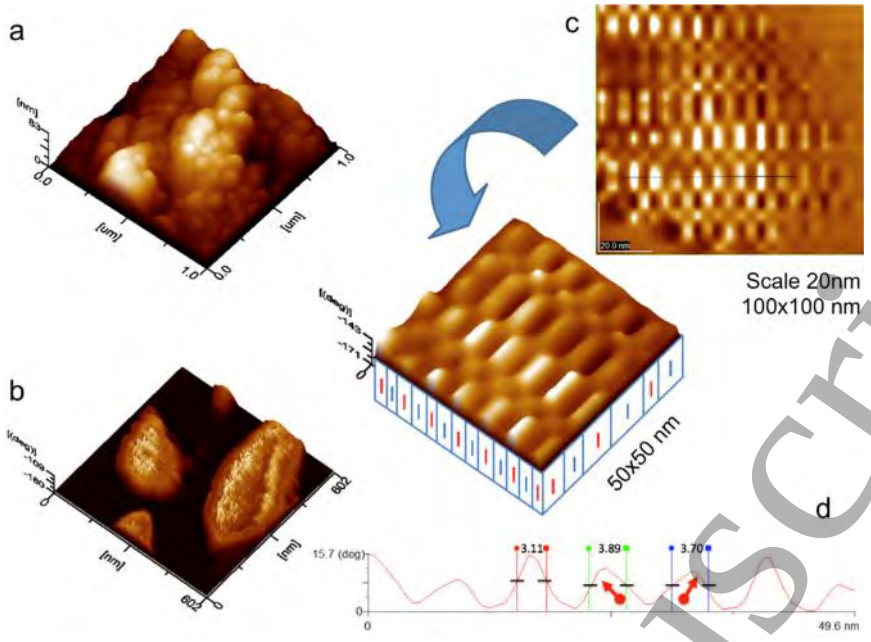

Figure 5. Magnetic domains in VP-MNPs: (a) Topography of Fe_3O_4@Fe_2O_3 magnetic nanoparticles; (b) Totally saturated individual MNPs; (c) Magnetic domains in the core region and orientation in response to the AC field (arrows), attractive (brighter zones) or repulsive (darker zones) interactions; (c) Projection of selected domains (dotted line) and their dimensions (d) in profile.

The magnetic properties of the samples as evaluated by AFM-MFM measurements showed real-time domain orientation of the single-domain MNPs under an AC magnetic signal (**Figure 5**). The average signal from magnetic domains showed the precession expected under ac fields as reflected in the topographic profiles (**Figure 5**d), and the uniaxial nature of magnetic domains shifted according to the attractive or repulsive responses with the MFM lift conditions. It can be seen that MNPs distribution changes depending on the tip magnetization, reflecting the dependence of the interaction on MNPs size and topography. Single domain Fe_3O_4@γFe_2O_3 MNPs can be aligned by an external magnetic field and return to the initial conditions. Figure S1 (see Supplementary Information) shows magnetic domains interactions and the expected orientation (inset of Figure S1) following the magnetic field. Profiles from the magnetic domains showed average domain sizes of 6 nm for C-MNPs sample, and about 3 nm for SV-MNPs and VP-MNPs samples. All domains displayed an uniaxial behavior following the patterns shown in figure S1-a3 and S1-b3. The topography exhibited agglomeration of the MNPs (figure 5-a) with interphase among domains (Figure S1-a2, b3). The AC field H ≥12000 Oe was applied until the MNPs showed a completely saturated state (Figure S2).

3.2. Power absorption measurements

The systematic study on the SPA dependence with applied field H_0 was performed to determine the best heating efficiency of the MNPs in water (Table I). The data were fitted with a field dependence $SPA = AH_0^{\lambda}$, where A is a constant depending on the initial magnetic susceptibility

of the MNPs and λ is a parameter that allows estimating the validity of the Linear Response Theory (45). The best fits yielded values λ=2.5±0.5 for SV-MNPs, λ= 2.7±0.4 for VP-MNPs and λ=2.4±0.4 for C-MNPs, closed to the value of λ=2 expected within the validity range of the Linear Response (Figure 6). The highest SPA values at *f*=570 kHz and H_0=23.9 kA/m were found for C-MNPs (SPA= 335.69 W/g), which also has the highest M_S value and a coercivity of H_C (see Table I). For VP-MNPs, having a wider particle size distribution, the values were consistently lower (SPA=233.96 W/g), and the lowest SPA values were observed for SV-MNPs (78.93 W/g). As the specific power absorption depends on the concurrent effects of particle size distribution and magnetic anisotropy, it is difficult to establish the origin of the lower SPA in SV-MNPs without a systematic analysis of the magnetic configuration in this sample.

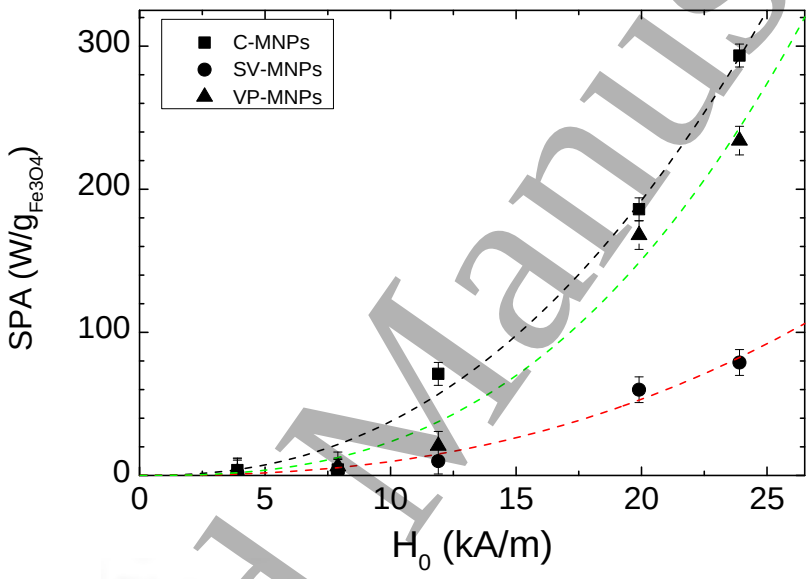

Figure 6. SPA dependence with applied magnetic field H_0 (*f*=570 kHz) for samples C-MNPs, SV-MNPs and VP-MNPs in water. Dashed lines are the best fits using $SPA = AH_0^{\lambda}$ for the three samples.

3.3. In vitro experiments of toxicity, uptaken and power absorption.

The toxicity of all MNPs in BV-2 cells, evaluated for concentrations up to 100 μg/ml of MNPs, showed that even at the highest concentrations all MNPs are remarkably innocuous for this cell line, showing in all cases cell viabilities higher than 94 % as compared with control cells (Figure S3 in Supplementary Information). These results suggest that the phenols at the particle surface constitute a natural camouflage that diminishes toxicity of MNPs comparing with non-coated Fe_3O_4 MNPs.

The uptake of both C-MNPs and VP-MNPs by BV2 cells after overnight incubation was also quantified as a function of added MNPs concentration (**Figure 7**).

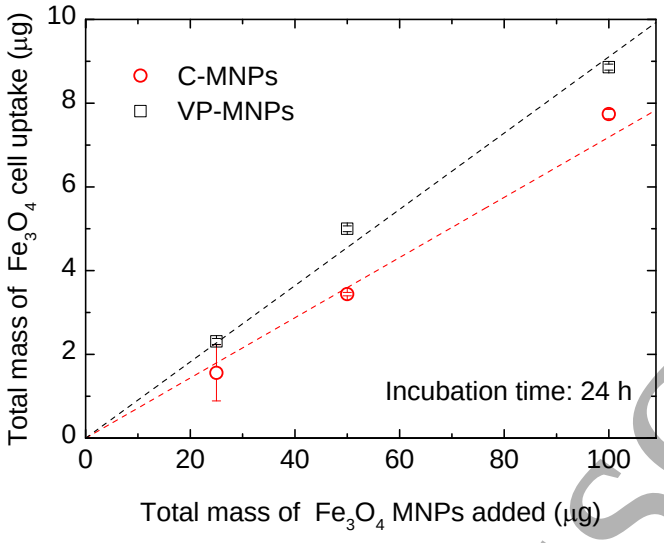

Figure 7. Cell uptake *vs* total amount of added Fe_3O_4@Fe_2O_3 MNPs (C-MNPs and VP-MNPs) at 24 h incubation time.

For both C-MNPs and VP-MNPs a linear increase of the uptaken mass with added concentration was found (**Figure 7**). The resulting concentration of MNPs was systematically higher for VP-MNPs than C-MNPs. A linear fit of the data using a linear $y = ax + b$ function (with $b = 0$) yielded values of $a = 0.091$ and $a = 0.071$ for VP- and C-MNPs, respectively. These uptake rates of 9% and 7% reflect the similarities in MNPs coatings in both cases. The mechanism for MNPs-cell membrane interaction can be related to the main components of cinnamaldehyde and vanillin in the extracts, which adds a negatively charged coating by the ionization of the exposed carboxylic groups (COO-) in VP-MNPs and partially hydrophobic surface in C-MNPs due to terpenoids. Their particle size and natural organic coating enhance their diffusion rates through the cell membrane aided by polyphenols and terpenoids that permeate easily (37, 62). DLS measurements indicated the formation of aggregates with hydrodynamic diameter (d_H) of 274 nm (σ=11.7) in VP-MNPs and larger agglomerates of d_H= 828 nm to 1.08 μm (σ =26.9) in C-MNPs. These agglomerates can be uptaken by BV2 cells since they show active uptake mechanisms of either agglomerated or non-aggregated MNPs.

The intracellular distribution of MNPs will be discussed in TEM section. Figure S4-a confirmed the formation of large intracellular clusters. Additionally, smaller agglomerates observed attached to the cell membrane, which could be due to the activation of polyphenol specific binding sites on the membrane (arrows in Figure S4-b), constituting the first step of an active endocytosis pathway (63).

3.4. Determination of SPA in BV-2 cell pellets.

Recent evidence indicates that physiological media (DMEM, cells viscosity) modifies nanoparticles hydrodynamic size due to their interaction with the constituent proteins and growth factors in cell culture media making up a "protein corona". These proteins attach to their surface increasing hydrodynamic radius and change mechanical properties. In order to determine the heating capacity of cinnamon and vanilla pods MNPs within the cell cytoplasm, a preliminary heating experiment was performed in cell pellets containing $\approx 1.5\times10^7$ cells. The obtained temperature vs. time heating profiles (Figure S5 in Supplementary Information) showed that for f=570 kHz and H_0= 23.9 k A/m the cells containing VP-MNPs the temperature increased up to hyperthermic values within the first seconds (43 ºC after 65 s), thus providing enough power absorption to perform the actual magnetic hyperthermia experiments to be performed. On the other hand, using the same number of cells with C-MNPs the hyperthermic threshold temperature (43 ºC) was achieved only after 430 seconds, with a maximum observed value of 53 ºC after 25 minutes. Consistently, the *in vitro* SPA values obtained from these experiments were SPA = 237 W/g and 118 W/g for in VP-MNPs and C-MNPs, respectively. Based on the above results the VP-MNPs were chosen as the more efficient system to develop the magnetic hyperthermia experiments *in vitro* described below.

3.5. Magnetic hyperthermia (MHT) in vitro.

To perform magnetic hyperthermia experiments in BV-2 cell line using the VP-MNPs the cells were cultured to ≈80% confluence and 100 μg of MNPs were added and incubated for 24 h. It is worth noting that this incubation time is shorter than the doubling time T_D=31.4 h determined for this cell line, and this fact assures that the intracellular MNPs concentration does not change due to cell duplication (46). After incubation, pellets containing >$1.8\text{x}10^7$ cells were suspended in 150 μl of completed culture media. A target temperature of T = 46 ºC was chosen and maintained during 30 minutes (f=570 kHz and H_0=23.9 kAm^{-1}) by feedback control of the magnetic field intensity. The MHT controls were established as follows: a) BV-2 cells without MNPs b) cells incubated with MNPs and no-MHT treated c) BV-2 cells without MNPs and treated to AMF d) cells incubated with MNPs and exposed to AMF for 30 minutes (Figure 8). Cell viability was assessed immediately (≈5 min) after the experiments and after 6 hour (t=6h) of reseeding the treated pellet.

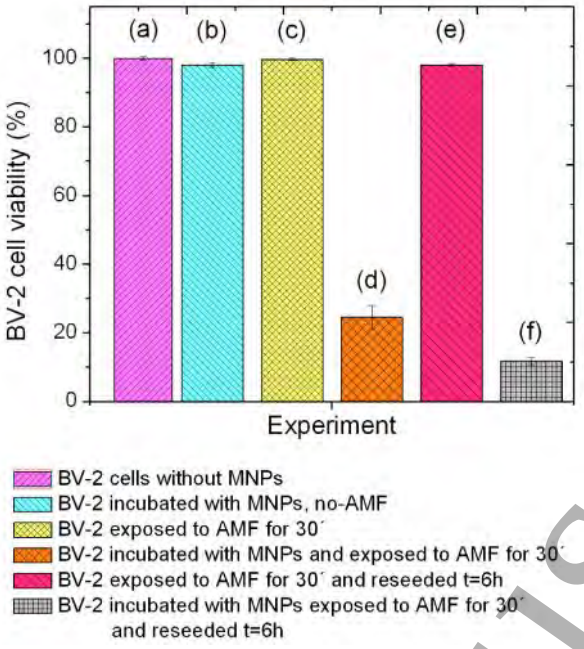

Figure 8. Magnetic hyperthermia on BV-2 cells. All experiments with VP-MNPs (100 μg/ml) were done in triplicate at f=571kHz, H_0=23.9 kAm^{-1} and target temperature T = 46 °C. Error bars are the mean standard deviation.

The results showed that the cell viability examined immediately after the MHT experiments decreases down to a 20% of survival as compared to control samples. Moreover, reseeding the cells and analyzing the viability after 6 h showed even lower cell viability (12%) reflecting the extent of cell damage induced by MHT on cell processes like cell division, organelles metabolic routes, protein denaturation among others. These findings are in agreement with recent results (64) observed after MHT on BV-2 cells and reseeding times of 4 h. Moreover, it has been suggested that these effects could be related to a "bystander effect" on neighbor cells after magnetically induced cell death (65). In all cases, control cells kept their viabilities up to 98-99%, ensuring that neither only MNPs nor AMF alone had an effect on cell viability.

Figures 9 and 10 show the sequence of the applied MHT in BV-2 cells. Where VP-MNPs inside cells were identified by EDS-X analysis (figure 9d). The MHT process from control to induced cell death was observed in TEM images. Figure 10a shows none-treated cells with unaltered morphology. Figure 10b, BV-2 cells incubated with VP-MNPs and none-AMF exposed. TEM images revealed large phagocytic vesicles and MNPs-clusters across the cytoplasm with a semi-homogenous distribution. BV2 cells after MHT treatment (Figures 10 c-i), some MNPs were arranged in large clusters (Figure 9a) and others dispersed along the cytoplasm (Figure 10c and 10f). Figure 9b SEM-FIB images, where MNPs-clusters (15-25 nm) inside lysosomes appeared partially digested. That diminishes their agglomeration as a consequence of their dipolar interactions. Others MNPs-clusters remained in transit to the cytoplasm and were distributed

along the cell membrane (arrows in Figure 9a). Those MNPs were embedded in the extracellular cell matrix and contributed to heat generation alike in viscous media (through torque force). The SPA in a pellet containing >$1.8x10^7$ cells indicated a heating efficiency of 800 W. As a result of the induced magnetic hyperthermia an increased denaturation process in cell membranes (Figure 10c-f) as well as organelles (Figure 10h) was observed.

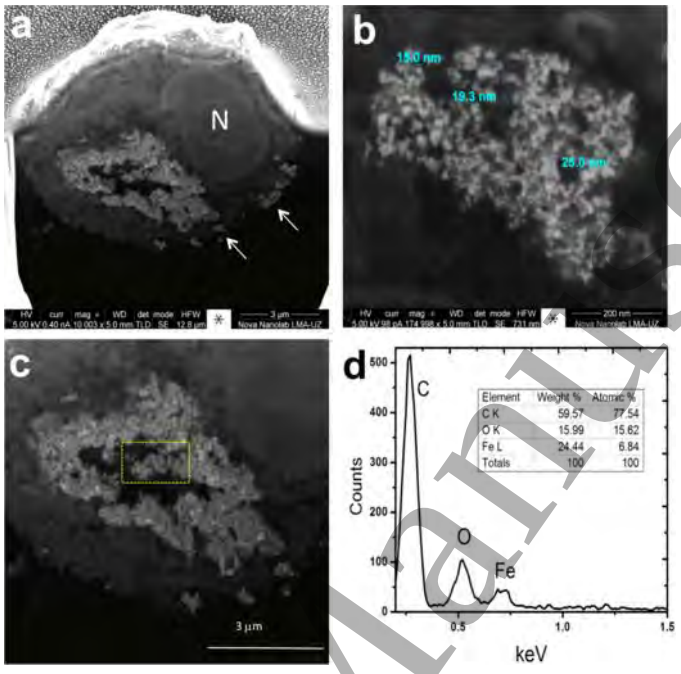

Figure 9. SEM-FIB images of (a) BV-2 cell after MHT at 46 °C (570 kHz, 23.9 kA/m) during 30 min, using VP-MNPs (100 µg/ml). The nucleus (N) is visible. The arrows signal the MNPs in transit from the cell membrane and into a phagosome. (b) Enlarged image from the intracellular agglomerate of MNPs shown in (c). (d) EDS-X spectra of the agglomerate area marked in (c) showing the absorption peak of iron from MNPs.

3.6. Ultrastructural morphological analysis of cell damage after MHT treatment.

The ultrastructure of BV-2 cells incubated with 100 µg/ml of VP-MNPs and exposed to f=570 kHz, H_0=23.9 kAm^{-1}, then reseeded for 6h was analyzed by TEM. The control cells with none-MNPS added displayed the normal cell ultrastructure (Figure 10a). Those exhibited numerous cell membrane extensions (filopodia), common feature of this macrophage-like immune brain cell. The organelles ultrastructure is well preserved. The nucleus occupies most of cytoplasm extension with a dense chromatin (heterochromatin) surrounding the nuclear cell membrane. This is interconnected with transcriptional active DNA regions less electrodense (euchromatin). The highly ordered ultrastructure of the nucleolus was observed as a large electrodense region. The control cells with added MNPs and non-MHT treated (Figure 10b), exhibited large cell membrane invaginations as a result of an active phagocytic process during the MNPs internalization. These invaginations in the cytoplasm were observed as some small lysosomes and large phagocytic vacuolae with numerous MNPs. The cell nucleolus exhibited an increased

size as a result of the activation of the molecular machinery for the synthesis of biomolecules required for MNPs digestion and signaling cascades of phagocytosis, endocytosis processes.

Cells incubated with MNPs and exposed to an AMF (Figures 10c-i) exhibited extended denatured areas in the cytoplasm. As a result organelles ultrastructure was disrupted with remnants surrounded by MNPs aggregates. The filopodia are absent due to cytoskeletal proteins denaturation during heating by MNPs. In some cells the cell membrane integrity was lost changing cells osmolality. As a result increased permeability induced cells swelling and membrane blebbing (arrows in Figure 10e). Then cells appeared to "burst" (alike necrosis), without releasing cytoplasm content. Inside those cells apoptotic bodies were observed (dotted squares in Figure 10c). In late apoptosis stage cell nucleus shrinks and finally it´s fragmented, leading to apoptotic bodies' formation (pyknotic nuclei). Some were observed among highly denatured cells in final apoptotic stages (Figure 10d).

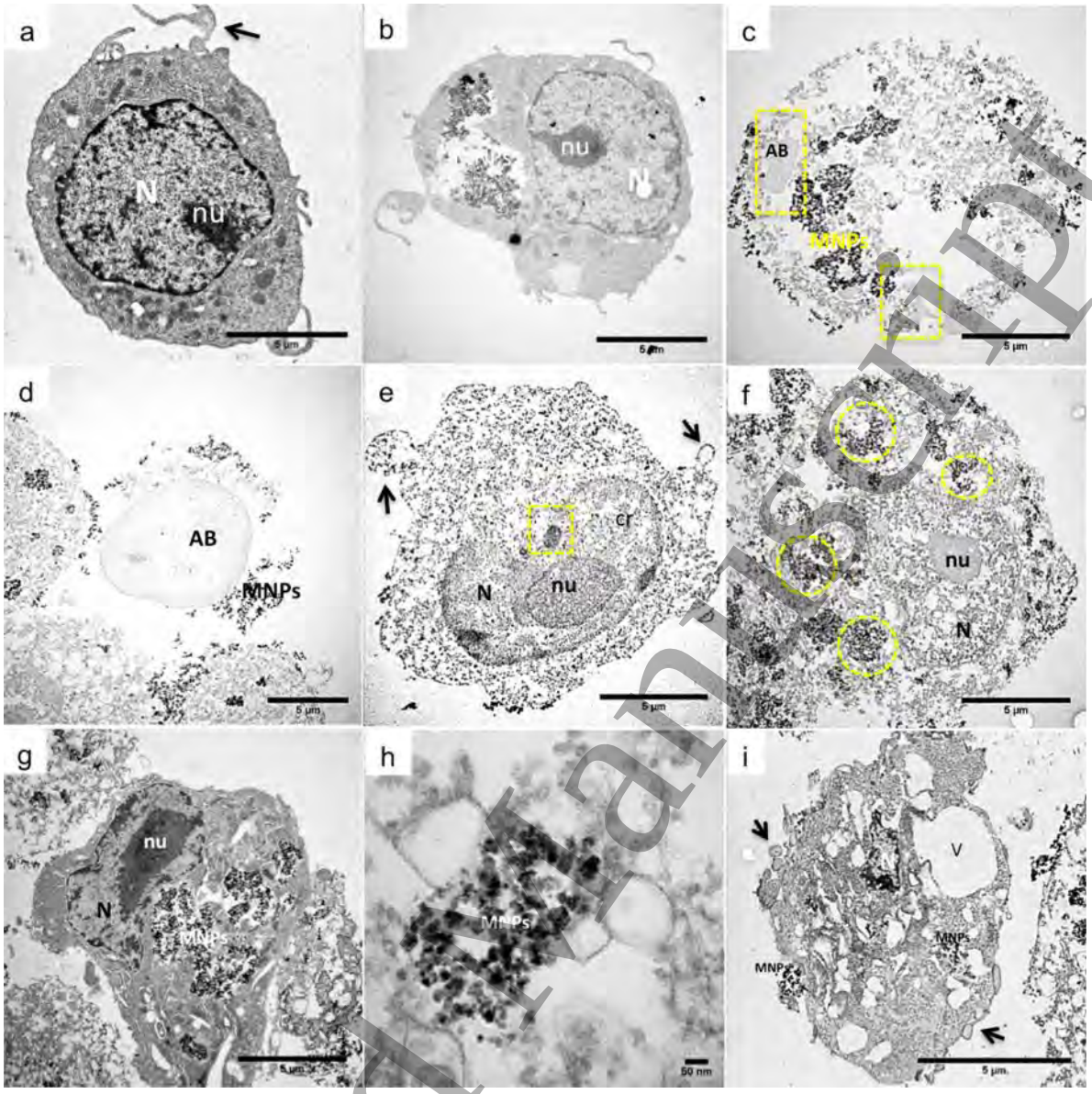

Figure 10. TEM images of BV-2 cells. (a) Control cell (b) incubated with 100 μg/ml of VP-MNPs and (c-i) MHT at 46 °C, 30 min, 570 kHz and 23.9 kA/m. Nucleus (N), nucleolus (nu), chromatin (cr), apoptotic bodies (AB), vacuolae (V). Magnetic nanoparticles (MNPs) surrounded by remnants of denatured organelles. See text description.

Other cells were shrunken with a highly vacuolated cytoplasm, small nuclei, and loss of filopodia to the periphery with the formation of membrane-bound fragments (arrows, Figure 10i). All these morphological changes of apoptotic cell death (66). In other cells highly chromatin condensation and decreased cell volume was observed, corroborating this cell death process.

In response to heat stress the synthesis of heat shock proteins (HSP) increases (67), and cell metabolic activity can be monitored trough nuclear chromatin packing and un-packing processes (square in Figure 10e) as well as in nucleolar morphology. In response to heat stress the constitutive level of genome transcription decreases and as a result nuclear chromatin is

packed in even denser regions (68). Nucleolus becomes transcriptionally active and enlarger due to the increased synthesis of molecular machinery for the transcription of HSP. This increase in size (Figures 10e-g) is associated with apoptotic cell death by hyperthermia (66, 68).

Among the cell population some appeared "non-damaged", (Figure 10g) but a closer inspection revealed an increased nucleolus metabolic activity as explained. The internalized MNPs appeared partially digested and organelles structurally damaged. Those alterations lead to a diminished response that alters the cell capacity to reestablish their metabolic functions as a consequence decreasing their survival (Figure 10f) after the MHT treatment (64). The level of damage is up to the distribution of MNPs along the cytoplasm and the formation of small dispersed (Figure 10f) or large agglomerates (Figure 10g). Those extensively distributed along cell cytoplasm exhibited more denatured areas, while those in a large cluster seemed not exerted an extensive intracellular damage but apoptotic features are more evident. However, all these ultrastructural changes suggest apoptotic and necrotic mechanisms for cell death.

4. Discussion

The genus *Cinnamomun* (family: Lauraceae) consists of 250 species of trees and shrubs distributed in South-east Asia, China and Australia. *C. verum* is native from Sri Lanka. Cinnamon is a small evergreen tree, 10-15m tall. The bark is used widely as a spice and as a preservative in food, due to their antioxidant property and antidiabetic agent a value-added product from cinnamon. The dried bark oil of cinnamon contains volatile oil, proanthocyanidins, tannins, proteins, pentosans, starch, calcium oxalate, mineral elements, eugenol and phenolic compounds (cinnamaldehyde, hydroxycinnamic acid) (69). The relative abundance of these components varies considerably according to location, age of the tree, climatic condition season time of harvest and duration of storage (70). Members of the genus *Cinnamomun* (*C. zeylanicum*) have been used to reduce silver, palladium and gold ions (71, 72). The reduction has been ascribed to the phenolic (euglenol), terpenoids, polysaccharides and flavones in the extract (73). Euglenol abundant in Tea green and eucalyptus extracts has been used to synthesize iron nanoparticles (23). Magnetite nanoparticles have been functionalized with synthetic cinnamaldehyde for magnetic hyperthermia to enhance breast cancer treatment (74). It has also been used to enhance the antimicrobial efficacy in chitosan/polyethylene oxide nanofibres against pseudomonas infections (37). The major chemical compounds of *Cinnamomun verum* extract are summarized in Figure 11.

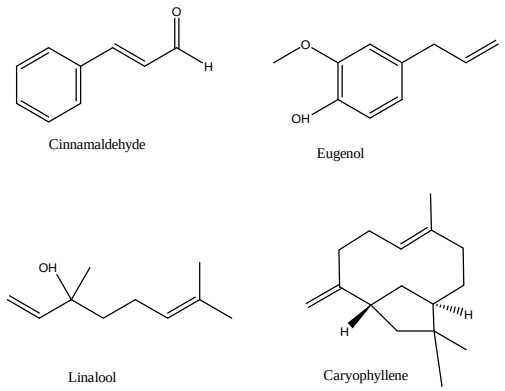

Figure 11. Structural formulae of main compounds in cinnamon extract.

(E)-cinnamaldehyde is the main organic compound in *Cinnamomun verum* (85-98%), followed by eugenol and trans-cinnamic acid (5-10%) according to Ooi et al. (75) and Tomas et al. (70). Due to the complex mixture of biomolecules in the extracts the mechanism of biosynthesis is not entirely clear yet. According to several researches (17) phenolic-OH groups and ortho-dihydroxyphenyl groups under the influence of basic-pH oxidize to quinone, which in instance donate their electrons from hydroxyl radical (-OH) to form a complex with metallic cations and reduce Fe^{2+}/Fe^{3+} ions to produce $Fe_3O_4@Fe_2O_3$ nanoparticles. The delocalized electrons in the aromatic ring potentiates the reduction reaction also donating their electrons, whereas organic acids carboxyl groups (-COOH) lose their hydrogen atom and become a carboxylate ion (COO-) during reduction. This mechanism stabilizes the electrosterical attachment to the nanoparticle's surface through organic chains (17). The bioreduction reaction can be represented as follows (76):

$$FeCl_3 + H_2O \rightarrow Fe[(H_2O)_n]^{3+} + H_2O \qquad \text{Eq.(1)}$$

$$R + Fe[(H_2O)_n]^{3+} + H_2O \rightarrow Fe[(H_2O)_n]^{2+} + H^+ + ROH \qquad \text{Eq.(2)}$$

$$Fe[(H_2O)_n]^{2+} + 2R^- + H^+ + OH^- \xrightarrow[\Delta]{pH} Fe^{2+}O^{2-} + Fe^{2+}Fe^{3+} + RH^+ROH^- \qquad \text{Eq.(3)}$$

Where "R" is the organic chain polyphenol -OH that yields the bioreduction of Fe atoms (Figure 12).

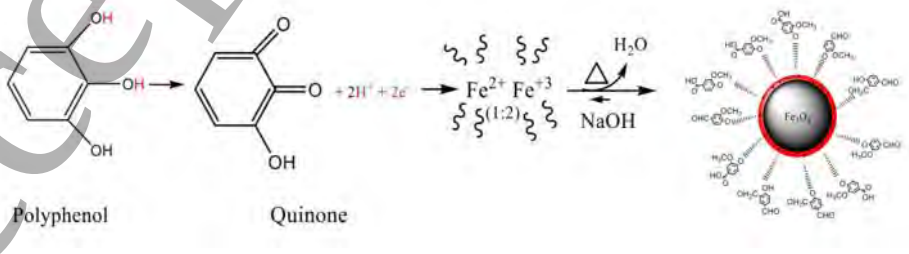

Figure 12. Scheme of chemical events during green synthesis. Polyphenols act as capping and bioreducing agents of iron cations. A partially oxidized nanoparticles surface of γ-Fe_2O_3 (red) with a Fe_3O_4 core is confined by polyphenols

in aqueous extract. Then base addition enhances the thermodynamic reaction to homogeneous iron nanoparticles precipitation.

Vanilla, a vine known since the Aztecs age, is a genus of about 110 species in the orchid family, an evergreen plant occurring in tropical and subtropical regions of tropical America, Asia, New Guinea and West Africa (77, 78). The main species for vanillin is *Vanilla planifolia*, native of Mexico but currently grown widely throughout the tropics. The major phenolic content in cured vanilla beans *V. planifolia* is vanilla, vanillic acid and 4-hydroxybenzaldehyde (78, 79) (Figure 13). Due to their antioxidant and antimicrobial properties vanillin is used as a food preservative (80). Vanillin is used as a starting material for the synthesis of L-dopa, for treating Parkinson's disease (79) and has been reported to assist the synthesis of silver nanoparticles (81).

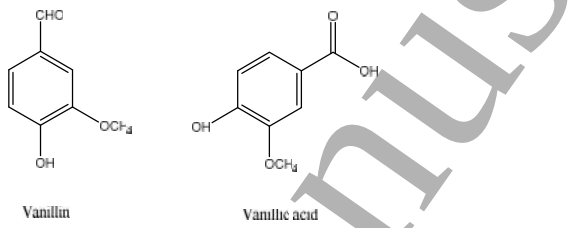

Figure 13. Structural formulae of phenols in vanilla pods.

These structures are similar poylphenols -OH like *C. verum* and the bioreduction mechanism would be the same. Considering cinnamaldehyde as a milder reducing agent (E^0=588 mV) (82) than vanillin (E^0=670-750 mV) (79), in electron transfer from their –OH groups during bioreduction. In our case *C. verum* and *V. planifolia* (natural and synthetic vanilla) aqueous extract assisted the formation and stabilization of Fe_3O_4@Fe_2O_3 nanoparticles by co-precipitation synthesis. Those were tested for hyperthermia in BV-2 microglia cells a model to research related neurodegenerative disorders (83).

Green syntheses as an ecofriendly alternative to chemical synthesis has been rarely explored regarding hyperthermia applications. It has been reported that biogenic magnetic iron nanoparticles like those from magneto-bacteria exhibit many good properties for biomedical applications, but their potential immunogenicity due to bacterial proteins surrounding the MNPs constitutes a drawback to be overcome before they can be safely applied to humans. Also solvent-based synthesis methods can produce MNPs with good heating performance (84, 85), but the by-side toxics generated from chemical reactions are rather hazardous and must be reduced in order to avoid environmental impact. In this regard, nanoparticles synthetized using plants aqueous extracts offer an experimental advantage to explore a less toxic synthesis of these materials, taking advantage of abundant biomolecules in nature related to oxidation-

reduction intracellular reactions. Among these biomolecules, polyphenols have been used to explore the biosynthesis of metallic nanoparticles (Au, Ag, Pt, Fe). Those have proved to be faster and simplified methodologies with higher nanoparticles yield production. Also in some cases diminish or replace the use of toxic organic solvents or neurotoxic reducing agents that assist nanoparticles synthesis, avoiding nanoparticles further processing for a biomedical application (19, 20). In order to explore this option we tested aqueous extracts from cinnamon (*Cinnamomum verum*), vanilla pods (*Vanilla planifolia*) and a commercial synthetic vanilla extract to assist the synthesis of MNPs. Due to their major polyphenols composition of cinnamaldehyde and vanillin, that aids the bioreduction of Fe^{2+}/Fe^{3+} ions and growth of MNPs. In our case a magnetic core of Fe_3O_4 surrounded by a layer of γ-Fe_2O_3 was synthesized. The global structural characterization by XRD confirmed the obtained phase with small changes in lattice parameters due to vacancies Fe^{2+} in the surface. It has a surrounding layer of biomolecules of polyphenol nature as indicated by FT-IR and TEM images.

The FT-IR values at 572 cm^{-1} of the obtained MNPs, are in accordance with those of Herrera-Becerra who reported a maximum absorption at 572 and 544 cm^{-1} for iron oxide nanoparticles synthetized with gallic acid and tannic acid, respectively (17). However other phytochemicals in the extract (i.e., vanilla extract), involved during the bioreduction process, must be kept in mind. Reports of the complex mixture in the extract suggest an elemental composition of reducing sugars such as β-D-glucosides (80). The partial reduction of $FeCl_3$ ions to obtain Fe_3O_4 nanoparticles has been reported using a highly abundant carbohydrate leaf extract of *Tridax procumbens* as reducing agents (86). In our case, the rich mixture in the extract requires further exploration.

The sizes obtained by this method were in the range of 10-14 nm. These nanoparticles exhibited a partially oxidized surface. Both characteristics have been reported to be in the size range (for magnetite) of good nanoheaters in liquid and viscous media (87), and the oxidized surface is more stable conferring high biocompatibility (88) for medical applications. In our case the synthesis method offers a particle size in the range of good heating performance and a bioactive surface to cells.

VSM analysis of their hysteresis loops indicated that all synthetized nanoparticles are near superparamagnetic. A comparison with similar methodologies of synthesis reported (54-61) that used bioreducing agents from aqueous plant extracts to obtain iron MNPs shows that those obtained with cinnamaldehyde had the highest saturation values (70.84 emu/g). These polyphenols act as an effective surface coating and add an evidence of their capacity as antioxidants (39). TEM observations suggested that the coating was not as wide as in vanilla synthesis, which is in agreement with their diminished saturation value (60 emu/g). The diminished magnetic saturation as a function of organic layer density has been reported elsewere (89). In our case, also influences the colloid behavior as DLS data showed the

formation of larger agglomerates in cinnamon (d_H=828nm-1.08μm) MNPs *vs* vanilla hydrodynamic radius (d_H=274 nm). The synthesis of larger ovoid forms observed by TEM in cinnamon extract could also contribute to the increased M_S (90).

The polyphenol-decorated surfaces constitute an effective coating that also improves biocompatibility, as inferred from cytotoxicity assays. The intracellular distribution and some MNPs-clusters attached to the cell membrane are consistent with the different stages of an active uptake process. Moreover, both endocytosis and phagocytosis pathways seem to be active since a fraction of the MNPs in the cytoplasm were found dispersed with no membranes as expected from a phagocytic mechanism; while the remaining fraction were agglomerated inside large phagocytic vesicles, consistent with endocytic mechanisms (63). Although size distributions could be improved in order to obtain more control on the final SPA values, in these magnetic materials the agglomeration during internalization is probably the main effect to be avoided, since their formation can largely influence SPA through dipole-dipole interactions.
These biomolecules of natural origin are a promising alternative to explore synergistic effect hyperthermia-cell damage as suggested by few reports (74). The synthesis of iron nanoparticles for hyperthermia using a chemical synthetized cinnamaldehyde has been made improving their bioactivity to breast cancer cells. Sensitizing cells to nanoparticles intake and inducing an apoptotic cell death (74). In our case natural vanillin as a bioactive molecule for MNPs cellular internalization as far as we concern has not been reported. Our exploration suggests their viability to achieve magnetic hyperthermia for the treatment of reactive BV2 cells as in neurodegenerative diseases or malignant brain processes.

5. Conclusions

In this work and eco-friendly synthesis was explored in order to obtain MNPs and their potential usage as nanoheaters. The main advantage of this method is to constitute a facile one-step synthesis of MNPs with sizes ≈10-14 nm, with a stabilized surface due to partial oxidation to γ-Fe_2O_3 (maghemite). The MNPs obtained showed the largest saturation magnetization values reported so far, with the additional advantage that the partial oxidation to γ-Fe_2O_3 of the MNPs surface, induced by natural polyphenols, increased particle stability. The SPA values *in vitro* were enough to reach up to 88% of cell death after 30 min application for VP-MNPs. The ultrastructural cell damage suggested that both apoptotic and necrotic processes could be triggered by MHT (~46 ^oC). Even though this synthesis employs natural sources for active biomolecules, improving the starting materials (e.g. highly purified aqueous extracts) could yet improve the synthesis control and therefore the heating performance. These results constitute a promising first step in ecofriendly-based low-cost synthesis routes of bioinspired systems. The

obtained MNPs are not only biologically safe and effective for biomedical uses, but also environmentally responsible.

Acknowledgments

This work was partially supported through Spain by the Ministerio de Economia y Competitividad (MINECO) project MAT2016-78201-P and the Aragon Regional Government (DGA, Project No. E26). Also, the authors want to express thanks to CONACyT (Mexico) for financial support to ALR-N through a PhD Student Exchange Program made at INA-UNIZAR. We are grateful to Dr. R. Fernández-Pacheco and Dr. T.E. Torres for their advice and technical support with TEM and Dual-Beam analysis, and to Dr. R. Cabreira for his help during VSM measurement. Technical support from Eng. M. Guerrero (CINVESTAV-IPN) during XRD characterization is acknowledged. We thank the LANE-CINVESTAV for the use of their AFM facilities.

References

1. Hasany F, Ahmed I, J R, Rehman A. Systematic Review of the Preparation Techniques of Iron Oxide Magnetic Nanoparticles. *Nanoscience and Nanotechnology*. 2013;**2**(6):148-58.
2. Andrés-Vergés M, Costo R, Roca AG, Marco JF, Goya GF. Uniform and water stable magnetite nanoparticles with diameters around the monodomain-multidomain limit. *Journal of Physics D: Applied Physics*. 2008;**41**(134008):1-10.
3. Plank C, Schillinger U, Scherer F, Bergemann C, Remy JS, Krotz F, et al. The magnetofection method: using magnetic force to enhance gene delivery. *Biol Chem*. 2003;**384**(5):737-47.
4. Tong L, Zhao M, Zhu S, Chen J. Synthesis and application of superparamagnetic iron oxide nanoparticles in targeted therapy and imaging of cancer. *Front Med*. 2011;**5**(4):379-87.
5. Asín L, Ibarra MR, Tres A, Goya GF. Controlled cell death by magnetic hyperthermia: Effects of exposure time, field amplitude, and nanoparticle concentration. *Pharmacological Research*. 2012;**29**:1319-27.
6. Swihart MT. Vapor-phase synthesis of nanoparticles. *Current Opinion in Colloid & Interface Science*. 2003;**8**(1):127-33.
7. Tadić M, Kusigerski V, Marković D, Panjan M, Milošević I, Spasojević V. Highly crystalline superparamagnetic iron oxide nanoparticles (SPION) in a silica matrix. *Journal of Alloys and Compounds*. 2012;**525**:28-33.
8. Arruebo M, Fernández-Pacheco R, Irusta S, Arbiol J, Ibarra MR, Santamaria J. Sustained release of doxorubicin from zeolite-magnetite nanocomposites prepared by mechanical activation. *Nanotechnology*. 2006;**17**:4057-64.
9. Tronc M, Jolivet R. Defect spinel structure in iron oxide colloids. *Materials Research Bulletin*. 1982;**17**:1365-9.
10. Kanitz A, Hoppius JS, Del Mar Sanz M, Maicas M, Ostendorf A, Gurevich EL. Synthesis of Magnetic Nanoparticles by Ultrashort Pulsed Laser Ablation of Iron in Different Liquids. *Chemphyschem*. 2017;**18**(9):1155-64.
11. Chen J, Wang F, Huang K, Liu Y, Liu S. Preparation of Fe_3O_4 nanoparticles with adjustable morphology. *Journal of Alloys and Compounds*. 2009;**475**(1-2):898-902.
12. Mizukoshi Y, Shuto T, Masahashi N, Tanabe S. Preparation of superparamagnetic magnetite nanoparticles by reverse precipitation method: contribution of sonochemically generated oxidants. *Ultrason Sonochem*. 2009;**16**(4):525-31.

13. Thakkar KN, Mhatre SS, Parikh RY. Biological synthesis of metallic nanoparticles. *Nanomedicine*. 2010;**6**(2):257-62.
14. Jamuna KS, Banu S, Brindha P, Kurian GA. Nano-scale preparation of Titanium dioxide by *Desmodium gangeticum* root aqueous extract. *Ceramics International*. 2014;**40**(8):11933-40.
15. Mittal AK, Chisti Y, Banerjee UC. Synthesis of metallic nanoparticles using plant extracts. *Biotechnol Adv*. 2013;**31**(2):346-56.
16. Gardea-Torresdey J, Tiemann K, González J, Henning J, Townsend M. Ability of silica-immobilized *Medicago sativa* (alfalfa) to remove copper ions from solution. *Journal of Hazardous Materials*. 1996;**48**:181-90.
17. Herrera-Becerra R, Rius JL, Zorrilla C. Tannin biosynthesis of iron oxide nanoparticles. *Applied Physics A*. 2010;**100**(2):453-9.
18. Mohanpuria P, Rana NK, Yadav SK. Biosynthesis of nanoparticles: technological concepts and future applications. *Journal of Nanoparticle Research*. 2007;**10**(3):507-17.
19. Herlekar M, Barve S, Kumar R. Plant-Mediated Green Synthesis of Iron Nanoparticles. *Journal of Nanoparticles*. 2014;**2014**:1-9.
20. Quester K, Avalos-Borja M, Castro-Longoria E. Biosynthesis and microscopic study of metallic nanoparticles. *Micron*. 2013;**54-55**:1-27.
21. Park Y, Hong YN, Weyers A, Kim YS, Linhardt RJ. Polysaccharides and phytochemicals: a natural reservoir for the green synthesis of gold and silver nanoparticles. *IET Nanobiotechnol*. 2011;**5**(3):69-78.
22. Marchiol L. Synthesis of metal nanoparticles in living plants. *Italian Journal of Agronomy*. 2012;**7**:274-82.
23. Wang T, Jin X, Chen Z, Megharaj M, Naidu R. Green synthesis of Fe nanoparticles using eucalyptus leaf extracts for treatment of eutrophic wastewater. *Sci Total Environ*. 2014;**466-467**:210-3.
24. Machado S, Pinto SL, Grosso JP, Nouws HP, Albergaria JT, Delerue-Matos C. Green production of zero-valent iron nanoparticles using tree leaf extracts. *Sci Total Environ*. 2013;**445-446**:1-8.
25. Gardea-Torresdey J, Gomez E, Peralta-Videa JR, Parsons JG, Troiani H, Jose-Yacaman M. Alfalfa sprouts: A natural source for the synthesis of silver nanoparticles. *Langmuir*. 2002;**19**:1357-61.
26. Njagi EC, Huang H, Stafford L, Genuino H, Galindo HM, Collins JB, et al. Biosynthesis of iron and silver nanoparticles at room temperature using aqueous sorghum bran extracts. *Langmuir*. 2011;**27**(1):264-71.
27. Genuino HC, Mazrui N, Seraji MS, Luo Z, Hoag GE. Green Synthesis of Iron Nanomaterials for Oxidative Catalysis of Organic Environmental Pollutants. *New and Future Developments in Catalysis*. Elsevier. 2013. p. 41-61.
28. Huang J, Li Q, Sun D, Lu Y, Su Y, Yang X, et al. Biosynthesis of silver and gold nanoparticles by novel sundried *Cinnamomum camphora* leaf. *Nanotechnology*. 2007;**18**:1-11.
29. Gardea-Torresdey J, Parsons J, Gomez E, Peralta-Videa J, Troiani H, Santiago P, et al. Formation and growth of Au nanoparticles inside live alfalfa plants. *American Chemical Society*. 2002;**2**(4):397-401.
30. Kharissova OV, Dias HV, Kharisov BI, Perez BO, Perez VM. The greener synthesis of nanoparticles. *Trends Biotechnol*. 2013;**31**(4):240-8.
31. Darroudi M, Hakimi M, Goodarzi E, Kazemi Oskuee R. Superparamagnetic iron oxide nanoparticles (SPIONs): Green preparation, characterization and their cytotoxicity effects. *Ceramics International*. 2014;**40**(9):14641-5.
32. Narayanan S, Sathy BN, Mony U, Koyakutty M, Nair SV, Menon D. Biocompatible magnetite/gold nanohybrid contrast agents via green chemistry for MRI and CT bioimaging. *ACS Appl Mater Interfaces*. 2012;**4**(1):251-60.
33. Vittorio O, Curcio M, Cojoc M, Goya GF, Hampel S, Lemma F, et al. Polyphenols delivery by polymeric materials: challenges in cancer treatment. *Drug Delivery*.2016;**24**(1):162-80.

34. Baptista FI, Henriques AG, Silva AM, Wiltfang J, da Cruz e Silva OA. Flavonoids as therapeutic compounds targeting key proteins involved in Alzheimer's disease. *ACS Chem Neurosci*. 2014;**5**(2):83-92.
35. Zanforlin E, Zagotto G, Ribaudo G. The Medicinal Chemistry of Natural and Semi-Synthetic Compounds Against Parkinson´s and Huntington´s Diseases. *ACS Chemical Neuroscience*. 2017;**8**(11):2356-68.
36. Balasubramanian S, Girija AR, Nagaoka Y, Iwai S, Suzuki M, Kizhikkilot V, et al. Curcumin and 5-Fluorouracil-loaded, folate- and transferrin-decorated polymeric magnetic nanoformulation: a synergistic cancer therapeutic approach, accelerated by magnetic hyperthermia. *International Journal of Nanomedicine*. 2014:**9**(1):437-59.
37. Rieger KA, Schiffman JD. Electrospinning an essential oil: cinnamaldehyde enhances the antimicrobial efficacy of chitosan/poly(ethylene oxide) nanofibers. *Carbohydr Polym*. 2014;**113**:561-8.
38. Silva GL, Lee I-S, Kinghorn AD. Special Problems with the Extraction of Plants. *In: Methods in Biotechnology*. Cannell R, editor. Vol. 4. Totowa, NJ: Humana Press; 1998. p. 343-63.
39. Kong KW, Mat-Junit S, Aminudin N, Ismail A, Adbul-Aziz A. Antioxidant activities and polyphenolics from the shoots of *Barringtonia racemosa* (L.) Spreng in a polar to apolar medium system. *Food Chemistry*. 2012;**134**:324-32.
40. M. Awwad A, M. Salem N. A Green and Facile Approach for Synthesis of Magnetite Nanoparticles. *Nanoscience and Nanotechnology*. 2013;**2**(6):208-13.
41. Santoyo-Salazar J, Castellanos-Roman M, Gómez-Looh B, Ihiawakrim D, Lefevre C, Pourroy G. Interactions of Magnetic Domains in Grain Boundaries and cores of Nanopolycrystalline Magnetite. J*ournal of Scanning Probe Microscopy*. 2009;**4**:17-23.
42. www.icdd.com.
43. Gupta AK, Gupta M. Cytotoxicity suppression and cellular uptake enhancement of surface modified magnetic nanoparticles. *Biomaterials*. 2005;**26**(13):1565-73.
44. Calatayud MP, Sanz B, Raffa V, Riggio C, Ibarra MR, Goya GF. The effect of surface charge of functionalized Fe3O4 nanoparticles on protein adsorption and cell uptake. *Biomaterials*. 2014;**35**(24):6389-99.
45. Sanz B, Calatayud MP, Cassinelli N, Ibarra MR, Goya GF. Long-Term Stability and Reproducibility of Magnetic Colloids Are Key Issues for Steady Values of Specific Power Absorption over Time. *European Journal of Inorganic Chemistry*. 2015;**2015**(27):4524-31.
46. Kim Jong Ah, Aberg Christoffer, Salvati Anna, A DK. Role of cell cycle on the cellular uptake and dilution of nanoparticles in a cell population. *Nature Nanotechnology*. 2012;**7**:62-8.
47. Iyengar SJ, Joy M, Ghosh CK, Dey S, Kotnala RK, Ghosh S. Magnetic, X-ray and Mössbauer studies on magnetite/maghemite core–shell nanostructures fabricated through an aqueous route. *RSC Adv*. 2014;**4**(110):64919-29.
48. Costo R, Bello V, Robic C, Port M, Marco JF, Puerto Morales M, et al. Ultrasmall iron oxide nanoparticles for biomedical applications: improving the colloidal and magnetic properties. *Langmuir*. 2012;**28**(1):178-85.
49. M. Boskovic, G.F. Goya, S. Vranjes-Djuric, N. Jovic, B. Jancar, Antic B. Influence of size distribution and field amplitude on specific loss power. *Journal of Applied Physics*. 2015;**117**(103903):1-6.
50. Nasrazadani S, Raman A. The application of infrared spectroscopy to the study of rust systems II. Study of cation deficiency in magnetite (Fe_3O_4) produced during its transformation to maghemite and hematite. *Corrosion Science*. 1993;**34**(8):1355-65.
51. Guin PS, Das S, Mandal P. Electrochemical reduction of quinones in different media: a review. *International Journal of Electrochemistry*. 2010;**2011**:1-22.
52. de Jager LS, Perfetti GA, Diachenko GW. Determination of coumarin, vanillin, and ethyl vanillin in vanilla extract products: liquid chromatography mass spectrometry method development and validation studies. *J Chromatogr A*. 2007;**1145**(1-2):83-8.
53. Narayanan KB, Sakthivel N. Green synthesis of biogenic metal nanoparticles by terrestrial and aquatic phototrophic and heterotrophic eukaryotes and biocompatible agents. *Advances in Colloid and Interface Science*. 2011;**169**:59-79.

54. Niraimathee V. Green synthesis of iron oxide nanoparticles from *Mimosa pudica* root extract. *International Journal of Environment and Sustainable Development*. 2016;**15**(3):227-40.
55. Mahdavi M, Namvar F, Ahmad MB, Mohamad R. Green biosynthesis and characterization of magnetic iron oxide Fe_3O_4 nanoparticles using seaweed (*Sargassum muticum*) aqueous extract. *Molecules*. 2013;**18**(5):5954-64.
56. Kumar B, Smita K, Cumbal L, Debut A. Biogenic synthesis of iron oxide nanoparticles for 2-arylbenzimidazole fabrication. *Journal of Saudi Chemical Society*. 2014;**18**(4):364-9.
57. Yan Cai, Yuhua Shen, Anjian Xie, Shikuo Li, Xiufang Wang. Green synthesis of soya bean sprouts-mediated superpatamagnetic Fe_3O_4 nanoparticles. *Journal of Magnetism and Magnetic Materials*. 2010;**322**:2938-43.
58. Adbeen M, Sabry S, Ghozlan H, El-Gendy AA, Carpenter EE. Microbial-physical synthesis of Fe and Fe_3O_4 magnetic nanoparticles using *Aspergillus niger* YESM1 and supercritical condition of ethanol. *Journal of Nanomaterials*. 2016;**2016**:1-7.
59. Venkateswarlu S, Subba Rao Y, Balaji T, Prathima B, Jyothi NVV. Biogenic synthesis of Fe_3O_4 magnetic nanoparticles using plantain peel extract. *Materials Letters*. 2013;**100**:241-4.
60. Venkateswarlu Sada, Kumar Natesh B, Prasad CH, Venkateswarlu P, Jyothi NVV. Bio-inspired green synthesis of Fe_3O_4 spherical magnetic nanoparticles using *Syzygium cumini* seed extract. *Physica B*. 2014;**449**:67-71.
61. Lee J, Roh Y, H H. Microbial production and characterization of superparamagnetic nanoparticles by *Schewanella sp.* HN-41. *Journal of Microbiology and Biotechnology*. 2008;**18**(9):1572-7.
62. Han YS, Bastianetto S, Dumont Y, Quirion R. Specific plasma membrane binding sites for polyphenols, including resveratrol, in the rat brain. *J Pharmacol Exp Ther*. 2006;**318**(1):238-45.
63. Adjei Isaac M, Sharma B, Labhasetwar Vinod. Nanoparticles: cellular uptake and cytotoxicity. Capco David G, Chen Y, editors. *In: Nanomaterial impacts on Cell Biology and Medicine*. New York: Springer; 2014. p 277.
64. Calatayud MP, Soler E, Torres TE, Campos-Gonzalez E, Junquera C, Ibarra MR, et al. Cell damage produced by magnetic fluid hyperthermia on microglial BV2 cells. *Nature Scientific Reports*. 2017;**7**(8627):1-16.
65. Calatayud M Pilar, Asin L, Tres A, Goya Gerardo F, Ibarra M Ricardo. Cell bystander effect induced by radiofrequency electromagnetic fields and magnetic nanoparticles. *Current Nanoscience*. 2016;**12**:1-12.
66. Zierler S, Klein B, Furtner T, Bresgen N, Lutz-Meindl U, Kerschbaum HH. Ultraviolet irradiation-induced apoptosis does not trigger nuclear fragmentation but translocation of chromatin from nucleus into cytoplasm in the microglial cell-line, BV-2. *Brain Res*. 2006;**1121**(1):12-21.
67. Ito A, Matsuoka F, Honda F, Kobayashi T. Heat shock protein 70 gene theraphy combined with hyperthermia using magnetic nanoparticles. *Cancer Gene Theraphy*. 2003;**10**(12):918-25.
68. Salucci S, Burattini S, Falcieri E, Gobbi P. Three-*dimensional* apoptotic nuclear behavior analyzed by means of Field Emission in Lens Scanning Electron Microscope. *European Journal of Histochemistry*. 2015;**59**(2539):202-6.
69. Cheng DM, Kuhn P, Poulev A, Rojo LE, Ann LM, Raskin I. *In vivo* and *in vitro* antidiabetic effects of aqueous cinnamon extract and cinnamon polyphenol-enhanced food matrix. *Food Chemistry*. 2012;**135**:2994-3002.
70. Peter KV, *Handbook of herbs and spices*. (New York: CRCPress). 2000. p 311.
71. Sathiskumar M, Sneha K, Kwak IS, Mao J, Tripathy S, Yun Y. Phyto-crystallization of palladium through reduction process using *Cinnamon zeylanicum* bark extract. *Journal of Hazardous Materials*. 2009;**171**:400-4.
72. Sathiskumar M, Sneha S, Won S, Cho C, Kim S, Yun Y. *Cinnamon zeylanicum* bark extact and powder mediated green synthesis of nano-crystalline silver particles and its bactericidal activity. *Colloids and Surfaces B: Biointerfaces*. 2009;**73**:332-8.

73. Kumar KM, Mandal BK, Kumar KS, Reddy PS, Sreedhar B. Biobased green method to synthesise palladium and iron nanoparticles using *Terminalia chebula* aqueous extract. *Spectrochimia Acta Part A: Molecular and Biomolecular Spectroscopy*. 2013;**102**:128-33.
74. Wani KD, Kadu BS, Mansara P, Gupta P, Deore AV, Chikate RC, et al. Synthesis, Characterization and *In Vitro* Study of Biocompatible Cinnamaldehyde Functionalized Magnetite Nanoparticles (CPGF Nps) For Hyperthermia and Drug Delivery Applications in Breast Cancer. *PLoS One*. 2014;**9**(9):1-13.
75. Ooi LS, Li Y, Kanm S-L, Wang H, Wong EY, Ooi VE. Antimicrobial Activities of Cinnamon Oil and Cinnamaldehyde from the Chinese Medicinal Herb *Cinnamomum cassia* Blume. *The American Journal of Chinese Medicine*. 2006;**34**(3):511-22.
76. Saif S, Tahir A, Chen Y. Green Synthesis of Iron Nanoparticles and Their Environmental Applications and Implications. *Nanomaterials*. 2016;**6**(209):2-26.
77. Anklam E. Authenticity of Vanilla and Vanilla extracts. Part 1: Comprehensive survey of the literature. European Commission Environment Institute, Food and Drug Unit. 1993:63.
78. Havkin-Frenkel D, Belanger FC. *Handbook of Vanilla Science and Technology*. Wiley-Blackwell. 2010. p 360.
79. Walton NJ, Mayer MJ, Narbad A. Vanillin. *Phytochemistry*. 2003;**63**(5):505-15.
80. Burri J, Graf M, Lambelet P, Löliger J. Vanillin: More than a Flavouring Agent-A Potent Antioxidant. *J Sci Agric*. 1989;48:49-56.
81. Aswathy B, Avadhani GS, Sumithra IS, Suji S, Sony G. Microwave assisted synthesis and UV–Vis spectroscopic studies of silver nanoparticles synthesized using vanillin as a reducing agent. *Journal of Molecular Liquids*. 2011;**159**(2):165-9.
82. Arteaga JF, Ruiz-Montoya M, Palma A, Alonso-Garrido G, Pintado S, Rodriguez-Mellado JM. Comparison of the simple cyclic voltammetry (CV) and DPPH assays for the determination of antioxidant capacity of active principles. *Molecules*. 2012;**17**(5):5126-38.
83. Stansley B, Post J, Hensley K. A comparative review of cell culture systems for the study of microglial biology in Alzheimer´s disease. *Journal of Neuroinflammation*. 2012;**9**(115):1-8.
84. Guardia Pablo, Di Corato Riccardo, Lartigue Lenaic, Wilhelm Claire, Espinosa Ana, García-Hernández Mar, et al. Water-soluble iron oxide nanocubes with high values of specific absorption rate for cancer cell hyperthermia treatment. *ACS Nano*. 2012;**6**(4):3080-91.
85. Marcos-Campos I, Asín L, Torres TE, Marquina C, Tres A, Ibarra MR, et al. Cell death induced by the application of alternating magnetic fields to nanoparticle-loaded dendritic cells *Nanotechnology*. 2011;**22**(205101):1-13.
86. Senthil M, Ramesh C. Biogenic synthesis of Fe_3O_4 nanoparticles using *Tridax procumbens* leaf extract and its antibacterial activity on *Pseudomonas aeruginosa*. *Digest Journal of Nanomaterials and Biostructures*. 2012;**7**(3):1655-60.
87. Fortin Jean-Paul, Gazeau Florence, Wilhelm Claire. Intracellular heating of living cells through Néel relaxation of magnetic nanoparticles. *European Biophysics Journal*. 2008;**37**:223-8.
88. de la Presa P, Luengo Y, Multinger M, Costo R, Morales MP, Rivero G, et al. Study of heating efficiency as a function of concentration, size, and applied field in γ-Fe_2O_3 nanoparticles. *The Journal of Physical Chemistry C*. 2012;**116**:25602-10.
89. Di Corato Riccardo, Espinosa Ana, Lartigue Lenaic, Tharaud Mickael, Chat Sophie, Pellegrino Teresa, et al. Magnetic hyperthermia efficiency in the cellular environment for different nanoparticle designs. *Biomaterials*. 2014;**35**:6400-11.
90. Goya Gerardo F, Grazú V, Ibarra M Ricardo. Magnetic Nanoparticles for Cancer Therapy. *Current Nanoscience*. 2008;**4**:1-16.

Nanotechnology

ACCEPTED MANUSCRIPT

In vitro magnetic hyperthermia using polyphenol-coated Fe_3O_4@γ-Fe_2O_3 nanoparticles from Cinnamomun verum and Vanilla planifolia: the concert of green synthesis and therapeutic possibilities

To cite this article before publication: A.L. Ramirez-Nuñez *et al* 2017 *Nanotechnology* in press https://doi.org/10.1088/1361-6528/aaa2c1